Wireless mm-Wave Chipless Pressure Sensor

Sandra Rodini⬡, *Graduate Student Member, IEEE*, Simone Genovesi⬡, *Senior Member, IEEE*,
Giuliano Manara⬡, *Life Fellow, IEEE*, and Filippo Costa⬡, *Senior Member, IEEE*

Abstract— An innovative passive wireless pressure sensor is proposed. The sensor is based on a millimeter-wave chipless tag operating in the *Ka*-band that works in combination with a dielectric superstrate. The tag consists of a frequency-selective surface (FSS) printed on an ultrathin support dielectric substrate that separates it from a ground plane. The superstrate is placed on top of the tag and encapsulated to obtain the pressure sensor. Applying pressure on the ground plane causes a shift of the resonance peak due to the change in effective permittivity. The proposed sensor can work with copolar and cross-polar interrogation and it is probed without background subtraction using only amplitude measurements. The interrogation system consists of two commercial horn antennas placed up to a distance of 64 cm from the tag and a vector network analyzer (VNA). The proposed sensor is modeled through an equivalent circuit model (ECM) to explain the working principle, it is analyzed with full-wave simulations, and finally fabricated and carefully characterized. This is, as far as we know, the first chipless pressure sensor with a reading range larger than 5 cm which is not equipped with external antennas.

Index Terms— Chipless radio frequency identification (RFID), effective permittivity, mm-wave tag, pressure sensors, wireless sensors.

I. INTRODUCTION

PRESSURE is one of the most investigated quantities in the scientific world and for this reason pressure sensors are extensively investigated [1]. Pressure sensors convert a physical quantity, pressure, defined as the ratio between a force and the area on which it acts, into an electrical signal. Precisely because of their universality, pressure sensors are required in a large number of applications ranging from the mechanical industry to aerospace [2], biomedical, wearable, soft robotic. Pressure sensors can be based on different physical phenomena such as capacitive, resistive, piezoelectric, and optical [3], [4]. In resistive ones [5], [6], the electrical resistance decreases with the pressure. Capacitive ones [7] usually consist of a dielectric placed between two electrodes. In piezoelectric ones [8], a pressure applied causes a polarization of the material. Optical sensors are typically based on the propagation of light into optical fibers [9] and the applied pressure determines

a variation in received light intensity. These sensors require a wired readout system which makes the sensor difficult to install and consequently increase installation costs and require active excitation. In recent years, various wireless pressure sensors have been proposed which typically use wired sensor configuration in connection to a radio frequency module such as Bluetooth, Wi-Fi, or radio frequency identification (RFID). RFID technology allows to create sensors that are completely wireless and do not require batteries. RFID pressure sensors are mainly divided into two categories: chip and chipless. In those equipped with the chip [10], [11], [12], the sensing functionality interfaces with the RFID module [13]. On the other hand, chipless RFID sensors do not possess any electronic component, and thus, the sensing functionality is entirely based on the response of a resonator. The impinging wave hits the tag and it is mainly backscattered at the resonant frequency of the resonator. The sensing functionality is given by the frequency shift of the resonance peak of the backscattered signal. This category of sensors is characterized by the absence of electronic components and batteries. SAW sensors fall in the chipless category as no additional electronics are needed but an external antenna is required to send data through radio frequencies [14], [15], [16]. For instance, the touch-mode pressure sensor translates externally applied pressure into changes in capacitance which affects the global reflected signal. The typical reading range of these devices is around 40 cm [16]. Other chipless pressure sensors are proposed in [17] and [18] where a dielectric resonator-loaded waveguide is interfaced with a horn antenna and the backscattered resonance signal is affected by the pressure applied to a pressure chamber connected to the resonator. In [19], an mm-wave pressure sensor is obtained in a circuit board using a CPW resonator and a silicon membrane. The application of a pressure determines a variation in the thickness of the membrane which in turn determines a variation in the scattering parameters. Another resonator configuration exploiting the properties of 3-D-printed substrates is proposed in [20]. Applying pressure on the resonator varies both the thickness of the polymeric substrate and the permittivity and consequently varies the resonance peak. However, in previous cases the resonator should be connected to cumbersome antennas to be transformed into a wireless device. Other chipless pressure sensors rely on *LC* resonators [21] and typically consist of a spiral resonator, whose resonant frequency is affected by pressure through the loading effect of a membrane. These pressure sensors have reached a high level of miniaturization and have been experimented for biomedical applications such as intraocular pressure sensors [22], [23], [24], [25]. In this case, the readout

system consists of a loop antenna, and the reading system is wireless but extremely short range, that is, in the order of 1 or 2 cm [24], [25]. In this work, a different configuration is used to realize a long-range chipless pressure sensor. The proposed structure relies on an mm-wave chipless resonator used in combination with a dielectric superstrate which introduces a capacitive loading. When pressure is applied in the backside of the tag where it is shield, a change in the resonant frequency of the mm-wave resonator can be observed by measuring it wirelessly with a couple of horn antennas at a distance of several tens of cm. The sensor is entirely based on the resonator and does not need externally connected antennas differently to other configurations typically proposed in the literature. An initial study of the pressure sensor principle has been conducted in [26] using a depolarizing configuration. However, only preliminary numerical results and experiments have been carried out. Here, a copolarized resonator is used to accurately detect the frequency shift and a rigorous circuit model of the structure aimed at explaining the operating principle of the wireless pressure sensor is proposed. Moreover, an extensive measurement campaign has been conducted with a careful analysis of the repeatability of the measurements and error estimation. This article is organized as follows. Section II shows an initial layout of the pressure sensor with a single resonance which is presented together with its equivalent circuit model (ECM) to clarify the working principle. Section III describes the final version of the pressure sensor consisting of a thin cavity and three resonances. Section IV describes the assembling procedure of the sensor, the measurement setup, and the experimental results. The section also reports the error analysis and a proposed decision scheme. Finally, Section V presents the conclusions.

II. Sensor Configuration and Wireless Pressure Detection Approach

The proposed pressure sensor is based on a passive chipless tag which is remotely interrogated in the far-field. The tag comprises a frequency-selective surface (FSS) printed on a thin layer (d_1) of Roger 3003 that separates the dipoles from a metallic ground plane. The FSS, the dielectric, and the ground plane form a resonant cavity which can be represented by a tank LC circuit [27]. Initially, the FSS is considered as an infinite surface whose unit cells are formed by a single dipole resonator with a finite thickness t. The tag is then loaded with a dielectric superstrate polycarbonate (PC) with a thickness equal to d_2. The schematic view of the pressure sensor is shown in Fig. 1(a). By interrogating the resonator with the field aligned with the dipole [see Fig. 1(b)], the resonance frequency can be observed in the amplitude profile of the backscattered signal since the resonator absorbs some of the impinging energy [28]. On the other hand, the same structure can also respond in cross-polarization if interrogated with the electric field forming a 45° angle with the dipole [27], [29], [30] [see Fig. 1(c)]. The copolar response is typically characterized by sharp deeps, whereas due to losses of the substrate and superstrate, the cross-polar response is characterized by less sharp peaks which may lead to a less precise determination of the resonance shift less precise. However, the cross-polar
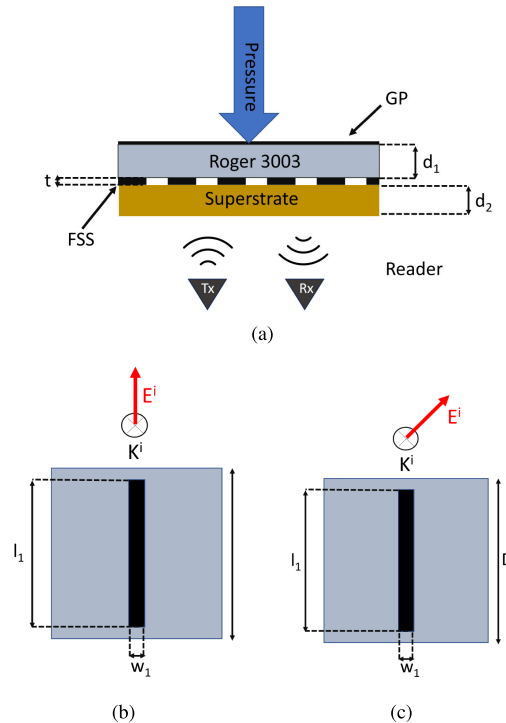

Fig. 1. (a) Schematic view of the proposed wireless pressure sensor ($t = 0.018$ mm, $d_1 = 0.5$ mm, and $d_2 = 0.75$ mm), (b) top view of the unit cell with FSS in the copolar configuration, and (c) top view of the unit cell of the FSS with the cross-polar configuration ($l_1 = 3.2$ mm, $w_1 = 0.035$ mm, and $D = 3.7$ mm).

configuration has the undoubted advantage of having more immunity with respect to the surrounding environment thus providing a much larger reading range as it will be demonstrated in the final part of the work. If a pressure is applied on the ground plane, thus without interfering with the RF interrogation, a shift of the resonant peak of the resonator is obtained. In the truncated configuration, a finite number of unit cells is selected and the amount of backscattered power depends on the total size of the resonator (the larger the resonator, the larger is its radar cross section (RCS). A tradeoff between achievable read range and sensor size is necessary in selecting the final number of unit cells: if a small sensor with short reading range is required, a small number of unit cells, that is, 2×2 or 3×3, is sufficient; if a reading range larger than 50 cm is needed, 5×5 or 10×10 configurations should be selected [27], [31].

A. Sensor Circuit Model

To better understand the operating principle of the sensor, its equivalent circuit can be considered. The Roger 3003 substrate and PC superstrate are modeled with a piece of transmission line with a length equal to d_1 and d_2, respectively. The equivalent circuit of the proposed pressure sensor is shown in Fig. 2. The FSS can be seen as an RLC series circuit. Our objective is calculate the circuit parameters of the FSS (R, C, and L) and then observe how these parameters change when a pressure is applied. Considering the circuit model in Fig. 2, the FSS impedance can be extracted as

$$Z_{\text{FSS}} = \frac{Z_{vr} Z_{vl}}{Z_{vr} - Z_{v_l}} \tag{1}$$

where

$$Z_{vl} = \frac{Z_{in} Z_2 - j Z_2^2 \tan(k_2 d_2)}{Z_2 - j Z_{in} \tan(k_2 d_2)} \quad (2)$$

with

$$Z_{in} = Z_0 \frac{1 + S_{11}}{1 - S_{11}} \quad (3)$$

and

$$Z_{vr} = j Z_1 \tan(k_1 d_1) \quad (4)$$

where d_1 and d_2 are the thickness of the Roger 3003 and the PC, respectively; k_0 is the free-space wavenumber ($k_0 = \omega(\varepsilon_0 \mu_0)^{1/2}$); and k_1 and k_2 are the wavenumber of the Roger 3003 and the PC, respectively. At this point, it is possible to consider the unit cell composed of the dipole. S_{11} is exported from full-wave simulations with a different filling factor F. The extracted impedance of the FSS is then approximated with RLC resonator as

$$Z_{FSS} = R + jwL + \frac{1}{jwC}. \quad (5)$$

Since the used dielectrics are lossy, a resistance in series with the capacitance and inductance is also included. According to the model, the values of the resistance, inductance, and capacitance of the FSS while different pressure is applied can be easily extracted using a simple fitting procedure [28]. Once the R, L, and C parameters are known, it is possible to compare the reflection coefficient obtained from the simulations and that obtained from the model. To obtain the reflection coefficient of the model, we use the classical $ABCD$ matrix approach [32]. The overall matrix of the system is given by the product of the matrices of the individual blocks. The dielectrics are represented as transmission line which are characterized by the $ABCD$ matrix

$$\begin{pmatrix} A_n & B_n \\ C_n & D_n \end{pmatrix} = \begin{pmatrix} \cos(k_n d) & j Z_n \sin(k_n d_n) \\ j \sin(k_n d)/Z_n & \cos(k_n d_n) \end{pmatrix} \quad (6)$$

where d represents the thickness of a generic nth dielectric layer, Z_n is the characteristic impedance of the generic dielectric, and k_n is the wavenumber of the material ($k_n = k_0 \sqrt{(\varepsilon_r \mu_r)}$). Finally, ε_0, ε_r, μ_0, and μ_r represent the free-space and the relative dielectric permittivities, and the free-space and relative magnetic permeabilities. On the other hand, lumped loads are represented by the following $ABCD$ matrix:

$$\begin{pmatrix} A & B \\ C & D \end{pmatrix} = \begin{pmatrix} 1 & 0 \\ 1/Z & 1 \end{pmatrix} \quad (7)$$

where Z represents the lumped impedance of a lumped load. It is replaced by Z_{FSS} or Z_{short}. In the ideal case, Z_{short} is zero, but in realistic case it assumes an extremely small value that can be evaluated as $Z_{short} = (1/\delta\sigma)$, where δ represents the skin depth of the metallic plane and σ its conductivity.

Once derived the complete $ABCD$ matrix of the system, it is possible to derive the reflection coefficient (S_{11}^{model}) of the circuit model

$$S_{11}^{model} = \frac{A Z_0 + B - C Z_0^2 - D Z_0}{A Z_0 + B + C Z_0^2 + D Z_0}. \quad (8)$$
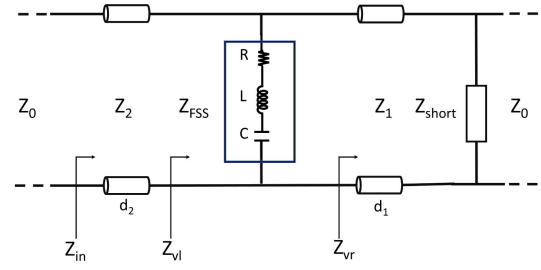

Fig. 2. ECM of the proposed chipless pressure sensor.

B. Sensor Physical Mechanism

To understand the physical mechanism of the proposed pressure sensor, electromagnetic numerical simulations were carried out using the CST Studio Suite Software. Since the dipoles are thick, there exist small air gaps between the FSS and the superstrate. As the applied pressure increases, the gaps are progressively filled with a consequent increase in the effective permittivity which in turn induces a variation in the FSS capacitance [33]. The change in the FSS capacitance determines a shift of the resonance peak. In simulations, to represent the case with no pressure applied, a simple contact between the tag and the superstrate is considered, and thus, air gaps between the tag and the superstrate exist. With the application of the pressure, the superstrate gradually fills the air gaps in different percentage. Fig. 3(a) shows two simulated configurations: the one in which the gaps filled of air and the one with the gaps are completely filled. To quantify the variation, the filling parameter F is defined

$$F = \frac{t - \Delta z}{t} \times 100 \quad (9)$$

where Δz represents the height of the air gap, and t is the metal thickness. In the absence of pressure, $\Delta z = t$ and the filling factor F will be equal to 0%. On the contrary, if the air gaps are completely filled as a consequence of the application of the pressure $\Delta z = 0$ and the filling factor will be equal to 100%.

The substrate is a layer of $d_1 = 0.5$ mm of Roger 3003 which is characterized by a relative dielectric permittivity equal to 3 and a tanδ equal to 0.001. The superstrate consists of a layer of PC with a relative dielectric permittivity equal to 2.5 and tanδ 0.03 with a thickness $d_2 = 0.75$ mm. The metal thickness t is equal to 0.018 mm. In Fig. 3(b) and (c), the reflection coefficient of the resonance peak as a function of the dielectric overlapping with the metallic traces is shown. The comparison is shown for both the copolar and cross-polar configurations. The cross-polar reflection in the circuit model is obtained using the matrix rotation approach discussed in [34]. The shift of the resonance peak determines a change in the capacitance in the ECM. The values of the capacitance, inductance, and resistance obtained from the ECM are also reported in Table I.

Considering that the inductance value is almost constant, it is possible to observe that the capacitance value increases linearly as with the filling factor F and therefore increases as a function of the applied pressure.
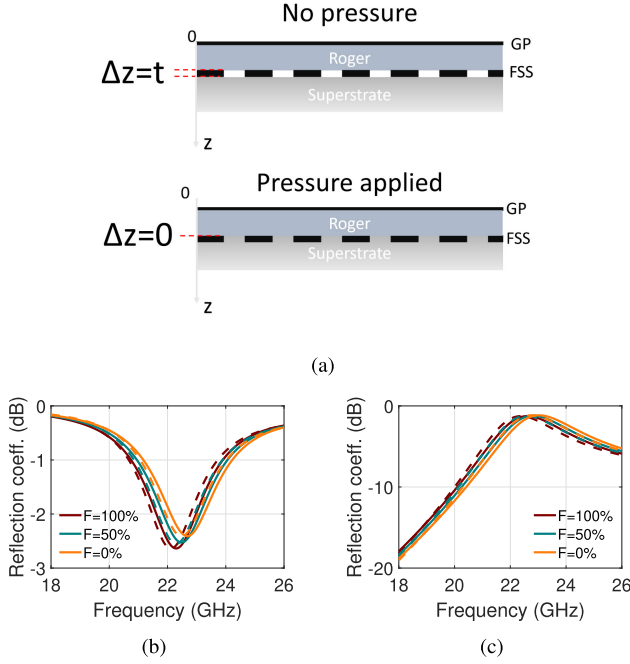
(a)

(b)

(c)

Fig. 3. (a) Scheme of the simulated configurations. Reflection coefficient of the resonance peak as a function of the dielectric overlapping in (b) copolar and (c) cross-polar configurations. The CST results (continue lines) are compared with those obtained with the ECM (dashed lines).

TABLE I
L, C, AND R PARAMETERS AS A FUNCTION OF THE FILLING FACTOR F

F (%)	L (nH)	C (fF)	R (Ω)
0	1.609	21,4	4.3
25	1.607	21,6	4.35
50	1.607	21,8	4.43
75	1.606	22,0	4.45
100	1.604	22,2	4.5

III. PRESSURE SENSOR DESIGN

The structure proposed in Section II shows a shift of the resonance peak as the applied pressure varies due to a variation in the value of the circuit capacitance which increases as the pressure increases. In the previous section, only an idea of the working principle of the sensor was shown. The Roger thickness of 0.5 mm is not a commercial thickness value; however, in simulation it was useful to use this value to explain the operating principle and also compute the equivalent circuit parameters. To have a deeper and sharper peak, a thinner Roger 3003 substrate can be used. Furthermore, it is here showed that a multiresonant structure can also be engineered to be able to have multiple frequency peaks. The new tag is characterized by an FSS composed of three dipoles with a thickness $t = 0.018$ mm, printed on a thin layer ($d_1 = 0.127$ mm) of Roger 3003 that separates the dipoles from a metallic ground plane. The three dipoles have different lengths (l_1, l_2, and l_3) to have different resonant peaks. The geometry of the unit cell is shown in Fig. 4(a), and the geometrical parameters are reported in Table II.

When a variable pressure is applied on the ground plane of the structure, a shift of the resonant peaks is observed. To understand the behavior of the new configuration, numerical electromagnetic simulations were carried out using the

TABLE II
GEOMETRICAL PARAMETERS FOR THE NEW CONFIGURATION OF THE PROPOSED PRESSURE SENSOR

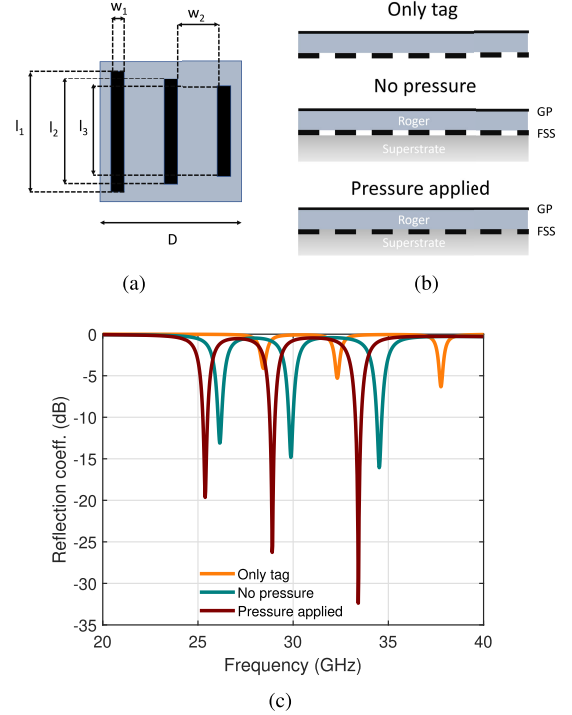| Parameter	Value (mm)	Parameter	Value (mm)
d_1	0.127	d_2	0.75
t	0.018	w_1	0.35
l_1	3.2	l_2	2.8
l_3	2.4	D	3.7

(a)

(b)

(c)

Fig. 4. (a) Unit cell of the new proposed chipless pressure sensor, (b) scheme of the simulations' configuration, and (c) results of the electromagnetic numerical simulation of the tag with three dipoles.

CST Studio Suite software. The simulation was performed in the frequency range between 20 and 40 GHz. The three cases described in Fig. 4(b) were considered. The first case is the one in which only the tag is present without the superstrate. The second case is where the superstrate is added but no pressure is applied. To have a configuration as similar as possible to the real one, it was considered that in the absence of applied pressure there was a small air gap of 0.005 mm between the tag and the superstrate due to the fact that the surface of the superstrate in reality is not perfectly flat. In this case between the tag and the superstrate, then there are air gaps. The third case is that following the application of pressure, the superstrate fills the air gaps. The three simulated configurations are shown in Fig. 4(b). In Fig. 4(c), the results of the numerical electromagnetic simulations are shown. For each peak, a variation in the resonance peak can be observed passing from the first to the third simulated case. In particular, a peak shift toward low frequencies is observed: 0.8 GHz, 1 GHz and 1.1 GHz for the first, second and third peak, respectively. According to our interpretation, the applied pressure leads to the filling of the air gaps between the FSS and superstrate. As a consequence, there is a downward shift in the resonance frequency due to the increase in the FSS capacitance.

The equivalent circuit of the final sensor configuration comprising the thin substrate and the three dipoles includes a series RLC resonator for each dipole, and the impedance of the FSS surface will be given by the parallel of the three series RLC branches [35].

Differently for the previous case where the substrate of the chipless tag was thicker, in this case of very thin substrate, the values of LC parameters are affected by the presence of the ground plane which is very close to the FSS. The reason is that the evanescent high-order Floquet modes of the FSS are not sufficiently attenuated [36].

IV. EXPERIMENTAL VALIDATION OF THE PROPOSED PRESSURE SENSOR

To validate the proposed sensor configuration, an extensive measurement campaign has been carried out.

A. Prototype Fabrication

The fabricated pressure sensor is shown in the inset of Fig. 5. The sensor comprises a chipless tag (FSS, Roger 3003, and ground plane) which is fabricated through a conventional photolitographic process and a polycarbonate superstrate which was placed on top of the FSS. The sensor has been encapsulated with tape.

B. Experimental Setup

An ad hoc measurement setup was designed to guarantee the application of a pressure in the small area of the sensor in a controlled way. To this purpose, the chipless sensor is placed on a polystyrene table in a reverse position where the superstrate is in contact with the table and the ground plane is on the top side. The polystyrene table has a minimal influence on the measurements as its permittivity is close to 1. A plastic tube is placed on top of the ground plane of the sensor and it is gradually filled with water to apply a controlled pressure. To avoid the random errors introduced by a manual water filling, a controlled and automated filling and emptying procedure has been adopted where a pump was used to fill the container and an electrovalve was used to gradually remove the water. The 12-V micro-pump and the electrovalve were connected to an USB relay which is connected to a power supply. The pump and the solenoid valve are activated for a suitable number of seconds to have filling and emptying of the desired quantity. Everything is automated and controlled via MATLAB. The water quantity used to apply pressure can also be converted into a pressure value according to these relationships

$$P = \frac{F}{A} \tag{10}$$

where

$$F = mg \tag{11}$$

with $g = 9.81$ m/s^2 and m is the mass of water in kilograms; and A is the area of the tag in square meter (the proposed sensor is characterized by an area of 3.7×3.7 cm^2).

To interrogate the sensor wirelessly, two commercial WR28 standard gain horn antennas operating in the frequency range
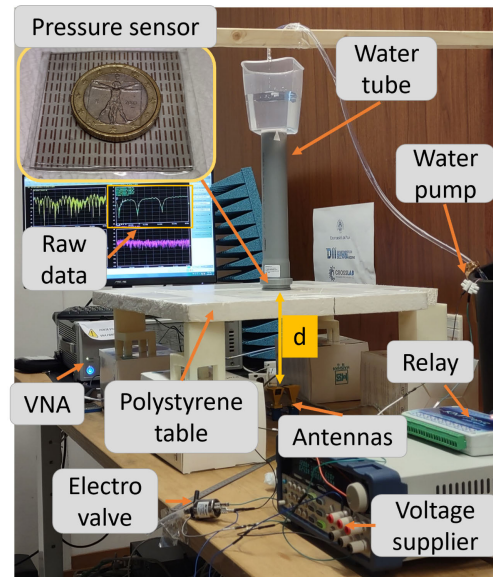

Fig. 5. Developed experimental measurement setup for characterizing the proposed chipless pressure sensor.
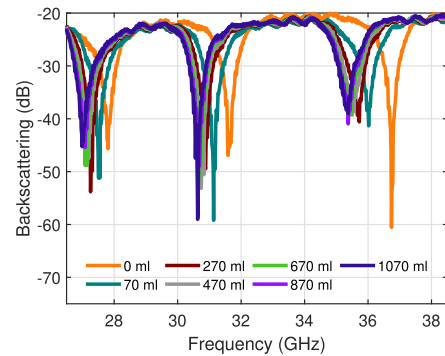

Fig. 6. Measured backscattering as a function of the applied pressure.

of interest (26–40 GHz) were placed below the polystyrene table to illuminate the sensor from the superstrate side. The antennas can be oriented so as to transmit and receive the same polarization or to receive cross-polarization. They were connected to an Anritsu Vector Network Analyzer (VNA) which operates up to 43 GHz. The measurement system is shown in Fig. 5.

C. Pressure Range Estimation and Calibration Curve

The first measurement consisted in measuring the sensor resting on the polystyrene support. The empty container is then placed on the sensor (it will exert an initial pressure that depends on its weight). The weight of the empty container is 70 g which roughly corresponds to 70 mL. Subsequently, 1 L of water is added at intervals of 100 mL. The measurements are repeated (ten times) to evaluate their repeatability and to assess the measurement uncertainty. The measured response of the sensor as a function of the applied pressure is shown in Fig. 6.

The proposed sensor has three resonance peaks, and therefore, each peak has been analyzed separately. The raw data of the measured backscattering (S_{21}) as a function of the applied
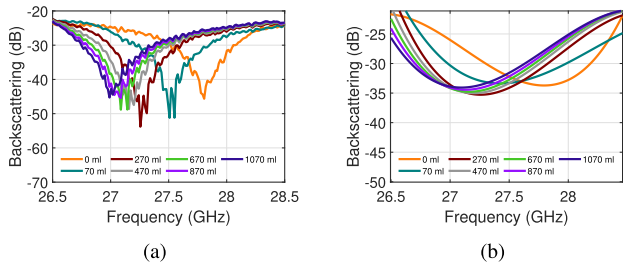
Fig. 7. Measured reflection coefficient of the proposed pressure sensor for the first resonance frequency. (a) Raw data and (b) processed data.
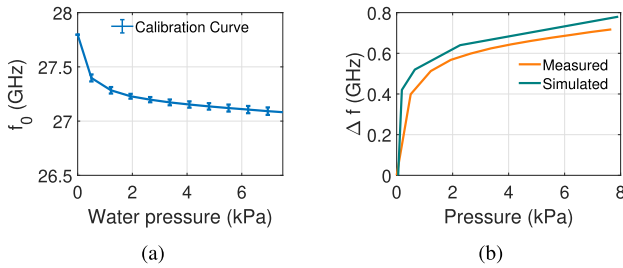

Fig. 8. (a) Calibration curve: variation in the resonance frequency of the first peak as a function of the applied pressure. (b) Comparison between the simulated and measured results.

pressure restricted in the frequency band of the first peak are shown in Fig. 7(a). It can be seen that the data have a jagged trend due to periodic oscillations which can be attributed to multiple reflections between the support table and the antenna. Although polystyrene has a dielectric permittivity close to 1, the table is considerably larger than the tag so even a small impedance mismatch produces some relevant reflections in the RCS. To calculate the frequency shift of the resonant peak of the sensor, a possible strategy consists in applying a polynomial approximation of the curve around the peak. An alternative strategy to remove the undesired oscillations consists in applying a time-domain filtering as it will be shown in the following sections. The postprocessed data are shown in Fig. 7(b). The curves show the same trend as before but are no longer jagged thus allowing to easily identify the minimum of the resonant curves. Each peak is processed with the same procedure and the frequency shift of all the resonant peaks is obtained.

To understand the operating range of the sensor, it is necessary to extract a calibration curve, that is, the shift of the resonance frequency (f_0) as a function of the pressure applied in kilopascal. Fig. 8(a) shows the sensor calibration curve relating to the first resonance peak. The calibration curve was obtained by averaging the ten repetitions carried out and the standard deviation is also reported. The low values of standard deviation indicate that the repeatability of the experiments is good. The maximum pressure value detectable with this measurement setup is equal to 7 kPa. It is observed that in the initial part the curve goes down very quickly while subsequently the variation in the resonance frequency with the variation in the volume of water is less steep. This indicates that the sensor is saturating.

The experimental calibration curve could be compared with the theory discussed in Section II. To compare the data, it is

necessary to find a relationship between the filling factor, used in simulations, and the applied pressure applied during experiments. Fig. 8 shows the comparison between the results obtained from the simulations and those obtained experimentally. The empirical relationship between the two quantities is the following:

$$P = e^{5*F}8/150$$

where P is the pressure value, and F is the filling factor.

D. Hysteresis Analysis

To study the behavior of the sensor in greater detail, we restrict to a smaller range of pressure values and the sensitivity of the pressure sensor is evaluated for smaller pressure steps. In particular, the container is filled with steps of 15 mL, that is, 0.11 kPa. In this experimental campaign, we consider a maximum volume of water equal to 300 mL which corresponds to a pressure of 2.15 kPa. Using a smaller amount of water, it was possible to carry out measurements both for filling and emptying phases, allowing us to make considerations on the overall cycles and one possible hysteresis behavior. In this case, the filling of the tube was carried out manually due to the limited precision of the adopted pump manually while emptying occurred via a valve connected to a small rubber tube placed at the base of the water container. The emptying method is more precise than filling as many random movements are generated during the experiments. The resonance frequencies (minima of the peaks) are computed for each level of applied pressure and then plotted in Fig. 9. The plots report the frequency shift of every resonant peak as a function of the applied pressure during the filling and emptying procedures. The curves also report the standard deviations since the experiments have been repeated three times to verify the repeatability of the process. From Fig. 9, it can be seen that although the start and end points corresponding to the minimum and maximum measured pressure are the same, the up and down curves are not overlapped. The deviation between the forward and backward curves seems to increase from the first to the third peak and reflects a hysteresis of the sensor. However, the deviation may also be partially attributed to the lower accuracy achieved in the filling experiments. The inaccuracy in controlling finely the applied pressure is also reflected into the standard deviations of the filling curves which are larger than those on the emptying curves. This also means that the measured standard deviations of the sensor may be overestimated for filling cycle. These residual random errors can be removed by automating the filling cycle using a pump with a finer control of the water flow (a smaller tube diameter is necessary to this purpose).

E. Decision Strategy and Error Assessment

To estimate the pressure, the relative frequency shift of the resonance frequency ($\Delta f_j/f_j$) of the peak j is considered. To estimate the pressure, it is possible to use one of the three resonant peaks separately (in this case a small frequency band is required for the reader) or it is possible to exploit all the three peaks together to improve the estimation. Two estimators will be therefore tested: the first one uses a single resonant
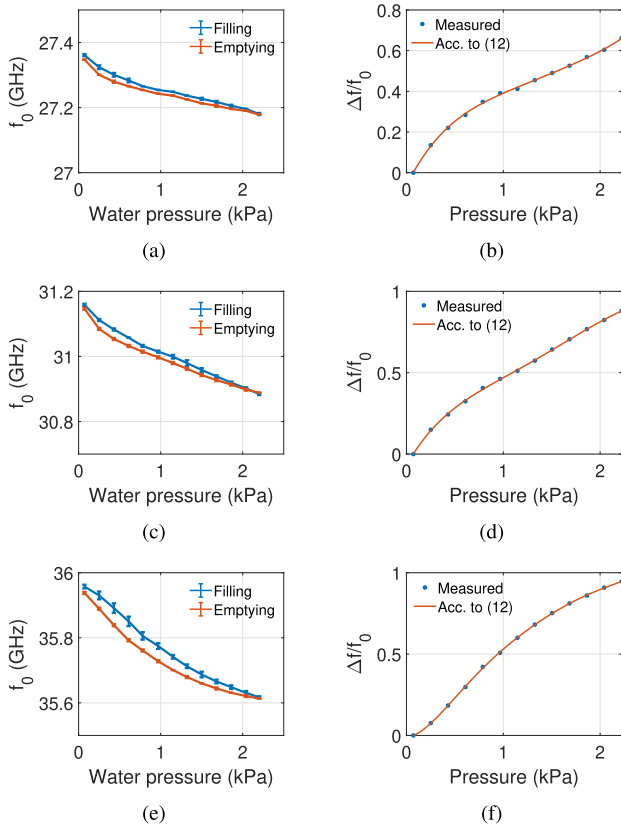
Fig. 9. Variation in the resonance frequency of the three peaks as a function of the applied pressure. (a) Peak 1, (c) peak 2, and (e) peak 3. Polynomial fitting for the three peaks (b) first peak, (d) second peak, and (f) third peak.

TABLE III
POLYNOMIAL COEFFICIENTS FOR THE THREE PEAKS

Coeff.	Peak 1	Peak 2	Peak 3
C_1	0.0056	0.0037	0.0468
C_2	-0.0164	-0.0108	-0.3801
C_3	0.0655	-0.0913	1.2432
C_4	0.04182	0.4994	-2.0690
C_5	0.8462	-0.9077	1.6694
C_6	0.9582	1.0443	0.0295
C_7	0.0631	-0.0687	-0.0097

an estimated pressure according to the calibration curve. This estimated pressure value for the nth realization and extracted from the peak j is called $\hat{P}_n^j$ where j represents the jth peak and n stands for the nth considered realization of the measurement dataset. The error related to peak j and the realization n is computed as

$$\text{err}_j^n = \left| \frac{\hat{P}_j^n - P_{\text{real}}}{P_{\text{real}}} \right| \times 100. \quad (13)$$

The overall error, for each pressure value, is given by the average of the error of n realizations as

$$\text{err}_j = \frac{\sum_{n=1}^{N} \text{err}_j^n}{N}. \quad (14)$$

An alternative decision strategy consists in considering the combination of the three peaks. In this case, the estimators rely on the estimated pressure $\hat{P}_{\text{comb}}^n$, which is obtained as the average of the pressures estimated on each peak according to

$$\hat{P}_{\text{comb}}^n = \frac{\sum_{j=1}^{J} \hat{P}_j^n}{J} \quad (15)$$

where $\hat{P}_j$ is the estimated pressure for each peak j and $J = 3$ in our case. The estimation error related to the combination of the three peaks can also be calculated similar to (16) where $\hat{P}_j^n$ is replaced by $\hat{P}_{\text{comb}}^n$

$$\text{err}_{\text{comb}}^n = \left| \frac{\hat{P}_{\text{comb}}^n - P_{\text{real}}}{P_{\text{real}}} \right| \times 100. \quad (16)$$

The average error for each pressure value, as in the previous case, is obtained by averaging the errors obtained in different realizations

$$\text{err}_{\text{comb}} = \frac{\sum_{n=1}^{N} \text{err}_{\text{comb}}^n}{N}. \quad (17)$$

Fig. 10 shows the estimation errors obtained with single peaks and with the combined approach using formula (14) and (17) multiplied by 100. For some pressure values, it would be more convenient to use the second peak, and in other cases (at high pressures) it would seem more convenient to use only the third peak. However, using a combination of the three the measurement error is always maintained below 5%.

F. Nonideal Environment

To study the robustness of the proposed sensor in realistic scenarios, its behavior in different surrounding environments is considered. This was done by placing different objects (metallic and nonmetallic) around the sensor. The response

peak (one out of three), whereas the second one merges all the data measured for the three peaks.

In case of a single peak, the estimation error is evaluated according to the following procedure: a dataset with three measurements for each peak, $\Delta f_j^n / f_j^n$, where j is the jth peak and n is the nth measurement for each pressure value is considered. The measurements represent multiple realizations of the random variable characterized by an average value and standard deviation. Based on the calibration curve of the sensor, it is possible to assess the percentage error of the pressure estimate for each one of the three measurements. To do that, it is necessary to increase the number of points of the calibration curve. This is obtained by approximating the experimental calibration curve shown in Fig. 9 with a polynomial function. From Fig. 9, it can be observed that the relative frequency shift ($\Delta f_j / f_j$) as a function of the applied pressure is perfectly approximated with a polynomial of degree 6. The polynomial that approximates the three peak calibration curves is a polynomial of the form

$$\Delta f_j / f_j = C_1 p^6 + C_2 p^5 + C_3 p^4 + C_4 p^3 + C_5 p^2 + C_6 p + C_7 \quad (12)$$

where C_n are the polynomial coefficients and are reported in Table III for each peak, and p is the pressure value expressed in kilopascal.

For each value of pressure in the dataset, the relative frequency shift for each individual realization ($\Delta f_j^n / f_j^n$) provides
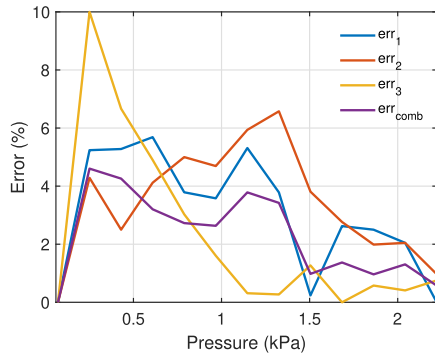
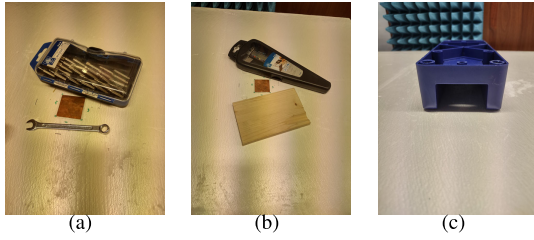Fig. 10. Error for single peaks and for the combination of the three peaks.

Fig. 11. Pictures of the three environments used to study the robustness of the proposed sensor. (a) Environment 1 (Env 1). (b) Environment 2 (Env 2). (c) Environment 3 (Env 3).
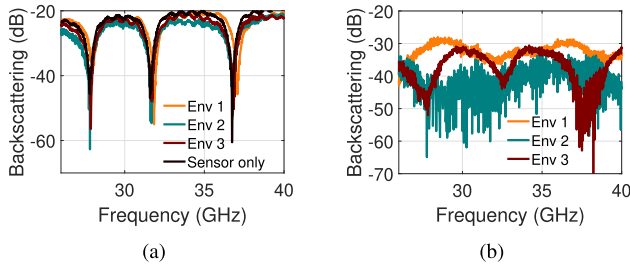

Fig. 12. (a) Sensor response under different environments. (b) Environment response.

of the investigated scenarios is evaluated in terms of RCS in the absence of the sensor. The pictures of the three different environments are shown in Fig. 11. In the first case, metal objects of considerable size are placed near the sensor. In the second case, metal and wood are located near the sensor while in the third case there is only a plastic object which entirely covers the sensor.

From Fig. 12, it can be observed that the presence of different objects around the sensor does not generally alter the resonant peak location. It is always possible to identify the three characteristic resonant peaks. The three environments can be characterized in terms of clutter level compared with the backscattering of the sensor itself. The signal-to-clutter ratio (SCR) values for the resonances are shown in Table IV. In the case of environment 1 in which there are metal objects, the clutter is greater but it is always possible to read the three resonance peaks. In the case of environment 2 where the clutter is very low, the SCR is high and the sensor only and $Env2$ curves are overlapped. It can be concluded that when the SCR is greater than 7 dB, it is still possible to identify the resonant peaks.

TABLE IV
SCR IN DECIBELS FOR EACH PEAK IN DIFFERENT ENVIRONMENTS

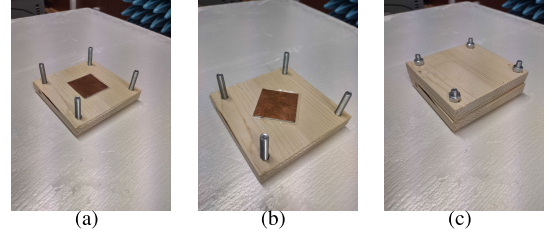| Env	SCR (f_1)	SCR (f_2)	SCR (f_3)
1	7	13	9
2	12	17	15
3	25	14	15

Fig. 13. Experimental setup used to emulate a practical application scenario. (a) Tag on wood in the copolar configuration. (b) Tag on wood in the cross-polar configuration. (c) Tag on wood with applied pressure.

G. Performance in Realistic Scenario

To evaluate the performance of the sensor in a realistic scenario, an additional measurement campaign was conducted. The proposed pressure sensor was placed between two wooden piles which can exert different pressure levels depending on the position of the four bolt screws placed on the four corners of the wooden plates. By tightening the screws, the two plates progressively move closer, and therefore, the pressure exerted on the tag increases. The measurements were carried out both in copolar and cross-polar and for different distances. The experimental setup is shown in Fig. 13.

The initial measurements have been carried out from 15 to 64 cm to evaluate the reading distance without applied pressure. In Fig. 14(a) and (b), the results of the measurements conducted at a distance of 27 cm are shown, while in Fig. 14(c) and (d) the backscattering at a distance of 64 cm is shown. In the copolar case, a considerable background noise due to the 10 cm² wooden plates is observed. At a distance of 27 cm, both the configurations (copolar and cross-polar) allow to discriminate the peaks and read the sensor. However, when the distance is equal to 64 cm, copolar data are no longer intelligible due to the background noise while it is still possible to discriminate the peaks using the cross-polar data. This is due to the fact that in the cross-polar configuration the clutter level is lower (around −75 dB) than the raw signal (−60 dB). In the copolar case, the background noise and the raw signal are comparable and it is not possible to discriminate the characteristic resonance peaks. Fig. 14 also shows alternative postprocessing strategies of measured data. The first strategy consists in subtracting the background from the raw data but in this case two measurements are required and it is not desirable in practical scenarios. However, comparing the raw data (raw) and background subtracted raw data (raw-bkg), no significant differences are observed indicating that background subtraction is unnecessary. Another postprocessing approach consists in performing an inverse Fourier transform (IFFT) of the measured data and applying a time gating widow to remove unwanted responses [37], [38]. Time-domain gating is found useful to smooth data representing a valid alternative to polynomial fitting presented

TABLE V
COMPARISON BETWEEN PRESSURE SENSORS

Reference	Operative range (GHz)	Pressure range (kPa)	Dimensions x-y-z (mm^3)	Reading range (cm)	Wireless	Sensitivity (MHz/kPa)	Resolution (kPa)
[17]	20-23	100-200	60×60×80	150	yes (with antennas)	4.55	40
[18]	17-21	0-200	40×40×90	50	yes (with antennas)	3.7	20
[19]	21-24	100-200	30×40× 20	-	no	6.20	50
[20]	8-12	0-60	30×30×20	-	no	0.14	/
[24]	0.32-0.38	0-13	4×1.5×1	2	yes	1.8	2.66
This work	25-40	0-7.15	37×37×0.8	64	yes	100	0.1
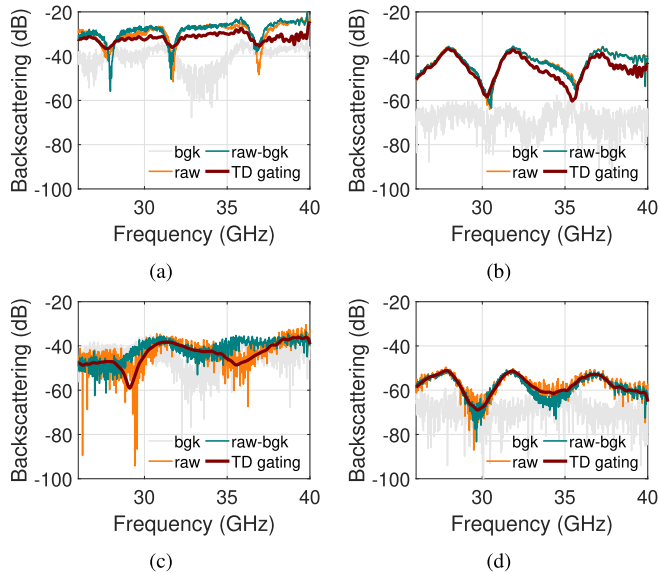
Fig. 14. Measured backscattering with the sensor embedded within wood piles of 2 cm. (a) Copolar, $d = 27$ cm. (b) Crosspolar, $d = 27$ cm. (c) Copolar, $d = 64$ cm. (d) Crosspolar, $d = 64$ cm.
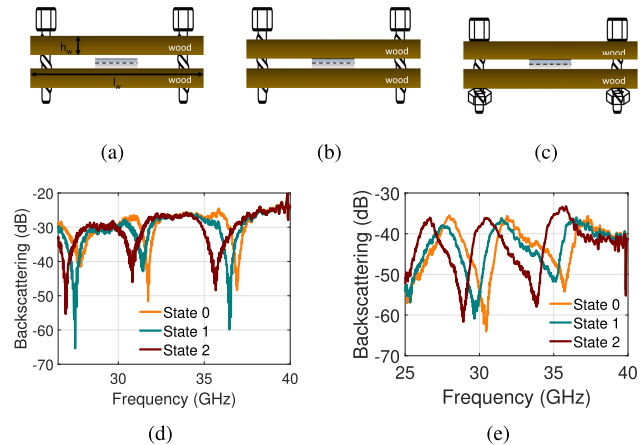

Fig. 15. Measurements configuration. (a) State 0, no pressure applied on the tag. (b) State 1. (c) State 2. (d) Measured backscattering in copolar at 27 cm. (e) Measured backscattering in cross-polar at 27 cm.

in previous sections. After the assessment of the reading range, the sensor has been placed between the two wooden plates and the bolts are progressively tightened. In the first configuration (State 0), the sensor is placed on the wooden plate and the second wooden plate is positioned above it without exerting pressure (the second plate does not touch the sensor). In state 1, the second plate touches the sensor, and thus, some pressure is applied. In state 2, the bolts are tightened and the maximum pressure is exerted on the tag. The results of these measurements are shown in Fig. 15. The distance between the antennas and the sensor is set to 27 cm to consider both copolar and cross-polar measurements. The frequency shifts observed in copolar and cross-polar measurements are the same even if higher uncertainty is encountered in the determination of the resonant point of the third peak using cross-polar data.

H. Literature Comparison

Table V shows a comparison between various passive and wireless pressure sensors available in the literature. It can be observed that all the pressure sensors with a reading range larger than 3 cm require the use of an antenna or a waveguide connected to the tag which ends up increasing drastically the volume of the sensor and its cost. The proposed pressure sensor allows to measure pressures ranging from 0 to 7.15 kPa from a distance up to 64 cm with a much smaller size and

cost. The pressure range could also be further widened by maintaining the same layout by modifying the used materials.

I. mm-Wave Reader

The use of mm-waves to design chipless pressure sensor is the possibility of obtaining considerable miniaturization of the device and also of the reader antennas. The sensor has been tested with laboratory equipment using a VNA but a portable reader is necessary to exploit the proposed sensor in practice. The design of an mm-wave reader may be more costly than a microwave reader but the efforts put by automotive industry in the recent years in developing mm-wave radars allowed to obtain tiny portable instruments with a cost well below 100 € [39]. The mm-wave radar is not at the moment devoted to detect frequency selective response of a target as it generally provides range-Doppler map only. However, since frequency-modulated continuous-wave (FMCW) radar interrogates the target with multiple tones, the detection of the frequency response is possible as demonstrated by some groups [40], [41], [42]. Other than commercial devices, other groups have designed FMCW radar with a considerable operation band (60–90 GHz) which can be used for the same purpose [43].

V. CONCLUSION

An mm-wave chipless sensor for pressure detection has been proposed. The sensor is composed by a periodic structure printed on a very thin grounded layer of Roger 3003. The

periodic surface comprises unit cells with three resonant dipoles which produces three resonant peaks in the backscattering profile. The resonant structure is loaded by applying a superstrate which determines a shift of the resonance peak as the pressure applied on the ground plane increases. The principle of operation of the sensor is initially illustrated using numerical electromagnetic simulations and the ECM. It has been shown how tag can work in both the copolar and cross-polar configurations. Subsequently, an ad hoc measurement setup was designed to test the sensor. A decision strategy based on a single peak or on multiple resonant peaks is presented and a decision error of 5% is evaluated. The sensor has also been characterized in nonideal environments and in realistic applicative scenarios showing the possibility of reading it up to 64 cm using the cross-polarized interrogation approach.

ACKNOWLEDGMENT

REFERENCES

[1] S. Jena and A. Gupta, "Review on pressure sensors: A perspective from mechanical to micro-electro-mechanical systems," *Sensor Rev.*, vol. 41, no. 3, pp. 320–329, Aug. 2021.

[2] L. Lin and W. Yun, "MEMS pressure sensors for aerospace applications," in *Proc. IEEE Aerosp. Conf.*, Mar. 1998, pp. 429–436.

[3] Y. Javed, M. Mansoor, and I. A. Shah, "A review of principles of MEMS pressure sensing with its aerospace applications," *Sensor Rev.*, vol. 39, no. 5, pp. 652–664, Sep. 2019.

[4] S. R. A. Ruth, V. R. Feig, H. Tran, and Z. Bao, "Microengineering pressure sensor active layers for improved performance," *Adv. Funct. Mater.*, vol. 30, no. 39, Sep. 2020, Art. no. 2003491.

[5] Y. Pang et al., "Flexible, highly sensitive, and wearable pressure and strain sensors with graphene porous network structure," *ACS Appl. Mater. Interfaces*, vol. 8, no. 40, pp. 26458–26462, Oct. 2016.

[6] C. Park et al., "Highly sensitive, stretchable pressure sensor using blue laser annealed CNTs," *Nanomaterials*, vol. 12, no. 13, p. 2127, Jun. 2022.

[7] Z. He et al., "Capacitive pressure sensor with high sensitivity and fast response to dynamic interaction based on graphene and porous nylon networks," *ACS Appl. Mater. Interfaces*, vol. 10, no. 15, pp. 12816–12823, Apr. 2018.

[8] W. Choi, J. Lee, Y. K. Yoo, S. Kang, J. Kim, and J. H. Lee, "Enhanced sensitivity of piezoelectric pressure sensor with microstructured polydimethylsiloxane layer," *Appl. Phys. Lett.*, vol. 104, no. 12, Mar. 2014, Art. no. 123701.

[9] Y. Zhu and A. Wang, "Miniature fiber-optic pressure sensor," *IEEE Photon. Technol. Lett.*, vol. 17, no. 2, pp. 447–449, Jan. 24, 2005, doi: 10.1109/LPT.2004.839002.

[10] C. Surman et al., "Temperature-independent passive RFID pressure sensors for single-use bioprocess components," in *Proc. IEEE Int. Conf. RFID*, Apr. 2011, pp. 78–84.

[11] A. Beriain, I. Rebollo, I. Fernandez, J. F. Sevillano, and R. Berenguer, "A passive UHF RFID pressure sensor tag with a 7.27 bit and 5.47pJ capacitive sensor interface," in *IEEE MTT-S Int. Microw. Symp. Dig.*, Jun. 2012, pp. 1–3.

[12] L. Catarinucci, R. Colella, and L. Tarricone, "Enhanced UHF RFID sensor-tag," *IEEE Microw. Wireless Compon. Lett.*, vol. 23, no. 1, pp. 49–51, Jan. 2013.

[13] F. Costa, S. Genovesi, M. Borgese, A. Michel, F. A. Dicandia, and G. Manara, "A review of RFID sensors, the new frontier of Internet of Things," *Sensors*, vol. 21, no. 9, p. 3138, Apr. 2021.

[14] G. Schimetta, F. Dollinger, and R. Weigel, "A wireless pressure-measurement system using a SAW hybrid sensor," *IEEE Trans. Microw. Theory Techn.*, vol. 48, no. 12, pp. 2730–2735, Dec. 2000.

[15] B. Dixon, V. Kalinin, J. Beckley, and R. Lohr, "A second generation in-car tire pressure monitoring system based on wireless passive SAW sensors," in *Proc. IEEE Int. Freq. Control Symp. Expo.*, Jun. 2006, pp. 374–380.

[16] J.-G. Oh, B. Choi, and S.-Y. Lee, "SAW based passive sensor with passive signal conditioning using MEMS A/D converter," *Sens. Actuators A, Phys.*, vol. 141, no. 2, pp. 631–639, Feb. 2008.

[17] P. Schumacher, C. Schuster, A. Jiménez-Sáez, M. Schüßler, and R. Jakoby, "Passive chipless wireless pressure sensor for harsh and reflective environments," in *Proc. 11th German Microw. Conf. (GeMiC)*, Mar. 2018, pp. 227–230.

[18] C. Schuster, P. Schumacher, M. Schüßler, A. Jiménez-Sáez, and R. Jakoby, "Passive chipless wireless pressure sensor based on dielectric resonators," in *Proc. IEEE SENSORS*, Oct. 2017, pp. 1–3.

[19] J. Philippe et al., "Passive and chipless packaged transducer for wireless pressure measurement," *Sens. Actuators A, Phys.*, vol. 279, pp. 753–762, Aug. 2018.

[20] K. R. Brinker and R. Zoughi, "Tunable chipless RFID pressure sensor utilizing additive manufacturing—Model, simulation, and measurement," *IEEE Trans. Instrum. Meas.*, vol. 72, pp. 1–13, 2023.

[21] Q.-A. Huang, L. Dong, and L.-F. Wang, "LC passive wireless sensors toward a wireless sensing platform: Status, prospects, and challenges," *J. Microelectromech. Syst.*, vol. 25, no. 5, pp. 822–841, Oct. 2016.

[22] C. C. Collins, "Miniature passive pressure transensor for implanting in the eye," *IEEE Trans. Biomed. Eng.*, vol. BME-14, no. 2, pp. 74–83, Apr. 1967.

[23] K. C. Katuri, S. Asrani, and M. K. Ramasubramanian, "Intraocular pressure monitoring sensors," *IEEE Sensors J.*, vol. 8, no. 1, pp. 9–16, Jan. 2008.

[24] P.-J. Chen, S. Saati, R. Varma, M. S. Humayun, and Y.-C. Tai, "Wireless intraocular pressure sensing using microfabricated minimally invasive flexible-coiled LC sensor implant," *J. Microelectromech. Syst.*, vol. 19, no. 4, pp. 721–734, Aug. 2010.

[25] L. Y. Chen et al., "Continuous wireless pressure monitoring and mapping with ultra-small passive sensors for health monitoring and critical care," *Nature Commun.*, vol. 5, no. 1, p. 5028, Oct. 2014.

[26] S. Rodini, Y. Zhao, S. Genovesi, G. Manara, and F. Costa, "A mm-wave depolarizing chipless pressure sensor," in *Proc. 17th Eur. Conf. Antennas Propag. (EuCAP)*, Mar. 2023, pp. 1–4.

[27] Y. Zhao, F. Soldi, S. Genovesi, G. Manara, and F. Costa, "Ultrathin and bendable mm-wave chipless tags based on grounded periodic surfaces," *IEEE Trans. Antennas Propag.*, vol. 71, no. 9, pp. 7661–7666, Sep. 2023.

[28] F. Costa, S. Genovesi, A. Monorchio, and G. Manara, "A circuit-based model for the interpretation of perfect metamaterial absorbers," *IEEE Trans. Antennas Propag.*, vol. 61, no. 3, pp. 1201–1209, Mar. 2013.

[29] A. Vena, E. Perret, and S. Tedjni, "A depolarizing chipless RFID tag for robust detection and its FCC compliant UWB reading system," *IEEE Trans. Microw. Theory Techn.*, vol. 61, no. 8, pp. 2982–2994, Aug. 2013.

[30] M. Borgese, F. Costa, S. Genovesi, and G. Manara, "Depolarizing chipless tags with polarization insensitive capabilities," *Electronics*, vol. 10, no. 4, p. 478, Feb. 2021.

[31] M. Borgese, S. Genovesi, G. Manara, and F. Costa, "Radar cross section of chipless RFID tags and BER performance," *IEEE Trans. Antennas Propag.*, vol. 69, no. 5, pp. 2877–2886, May 2021.

[32] D. M. Pozar, *Microwave Engineering*. Hoboken, NJ, USA: Wiley, 2011.

[33] F. Costa, "A simple effective permittivity model for metasurfaces within multilayer stratified media," *IEEE Trans. Antennas Propag.*, vol. 69, no. 8, pp. 5148–5153, Aug. 2021.

[34] M. Borgese and F. Costa, "A simple equivalent circuit approach for anisotropic frequency-selective surfaces and metasurfaces," *IEEE Trans. Antennas Propag.*, vol. 68, no. 10, pp. 7088–7098, Oct. 2020.

[35] F. Costa, S. Genovesi, and A. Monorchio, "A chipless RFID based on multiresonant high-impedance surfaces," *IEEE Trans. Microw. Theory Techn.*, vol. 61, no. 1, pp. 146–153, Jan. 2013.

[36] F. Costa, A. Monorchio, and G. Manara, "An equivalent-circuit modeling of high impedance surfaces employing arbitrarily shaped FSS," in *Proc. Int. Conf. Electromagn. Adv. Appl.*, Sep. 2009, pp. 852–855.

[37] A. Ramos, E. Perret, O. Rance, S. Tedjini, A. Lázaro, and D. Girbau, "Temporal separation detection for chipless depolarizing frequency-coded RFID," *IEEE Trans. Microw. Theory Techn.*, vol. 64, no. 7, pp. 2326–2337, Jul. 2016.

[38] F. Costa, S. Genovesi, and A. Monorchio, "Normalization-free chipless RFIDs by using dual-polarized interrogation," *IEEE Trans. Microw. Theory Techn.*, vol. 64, no. 1, pp. 310–318, Jan. 2016.

[39] V. Winkler, "Range Doppler detection for automotive FMCW radars," in *Proc. Eur. Microw. Conf.*, 2007, pp. 166–169.

[40] Q. Zhang, C. Zou, and L. Jiao, "Chipless tag detection and recognition based on frequency modulated continuous wave," *J. Phys., Conf.*, vol. 1972, no. 1, Jul. 2021, Art. no. 012015.

[41] J. Sánchez-Pastor, L. Piotrowsky, A. Jiménez-Sáez, M. Schüßler, N. Pohl, and R. Jakoby, "Evaluation of chipless RFID indoor landmarks at 80 GHz and 240 GHz using FMCW radars," in *Proc. 16th Eur. Conf. Antennas Propag. (EuCAP)*, Mar. 2022, pp. 1–4.

[42] M. Khaliel, T. Kaiser, K. Solbach, and A. El-Awamry, "Long range chipless RFID system based on FMCW RADAR and dielectric resonators," in *Proc. Int. Telecommun. Conf. (ITC-Egypt)*, Egypt, Jul. 2023, pp. 446–450.

[43] J. Barowski et al., "Design and evaluation of a passive frequency-coded reflector using W-band FMCW radar," in *Proc. German Microw. Conf. (GeMiC)*, Mar. 2020, pp. 92–95.

Sandra Rodini (Graduate Student Member, IEEE) received the B.Sc. and M.Sc. degrees in biomedical engineering from the University of Pisa, Pisa, Italy, in 2016 and 2019, respectively, where she is currently pursuing the Ph.D. degree in information engineering.

Her current research interests include radio frequency characterization of materials and design of wireless sensors.

Ms. Rodini was a recipient of the Young Scientist Award of the URSI International Symposium on Electromagnetic Theory, URSI General Assembly in 2021, and URSI AT-RASC in 2022. She was also a recipient of the Fourth Prize in the Student Paper Competition during the URSI-GASS 2021.

Simone Genovesi (Senior Member, IEEE) received the Laurea degree in telecommunication engineering and the Ph.D. degree in information engineering from the University of Pisa, Pisa, Italy, in 2003 and 2007, respectively.

From 2004 to 2006, he was a Research Associate at the ISTI Institute of the National Research Council of Italy (ISTI-CNR), Pisa. From 2015 to 2017, he was several times a short-term Visiting Researcher at the Grenoble Institute of Technology, Valence, France, and University Rovira I Virgili, Tarragona, Spain. Since 2003, he has been collaborating with the Electromagnetic Communication Laboratory, The Pennsylvania State University (Penn State), University Park, PA, USA. He is currently an Associate Professor with the "Dipartimento di Ingegneria dell'Informazione," University of Pisa. He is a Coordinator of the Additive Manufacturing Founded in the Framework of the Departments of Excellence ("Dipartimenti di Eccellenza") funded by the Italian Ministry of Education, University and Research. His current research interests include additive manufacturing, sensors, radio frequency identification (RFID) systems, and reconfigurable antennas.

Prof. Genovesi is an Associate Editor of IEEE TRANSACTIONS ON ANTENNAS AND PROPAGATION.

Giuliano Manara (Life Fellow, IEEE) is currently a Professor with the School of Engineering, University of Pisa, Pisa, Italy. Since 1980, he has been collaborating with the Department of Electrical Engineering, Ohio State University, Columbus, OH, USA, where, in the summer and fall of 1987, he was involved in research at the ElectroScience Laboratory, Columbus. His research interests include mainly the asymptotic solution of radiation and scattering problems to improve and extend the uniform geometrical theory of diffraction. He has also been engaged in research on numerical, analytical, and hybrid techniques (both in frequency and time domains), scattering from rough surfaces, frequency-selective surfaces (FSSs), and electromagnetic compatibility. More recently, his research has also been focused on the design of microwave antennas with application to broadband wireless networks, on the development and testing of new microwave materials (metamaterials), and on the analysis of antennas and propagation problems for radio frequency identification (RFID) systems.

Prof. Manara was elected an IEEE Fellow in 2004 for "contributions to the uniform geometrical theory of diffraction and its applications." In August 2008, he was elected the Vice-Chair of the International Commission B "Fields and Waves" of URSI (International Radio Science Union). He served as the International Chair for URSI Commission B for the triennium 2011–2014. He has been elected a URSI Fellow in 2017. Since 2021, he has been serving as the Vice-President for URSI.

Filippo Costa (Senior Member, IEEE) received the M.Sc. degree in telecommunication engineering and the Ph.D. degree in applied electromagnetism from the University of Pisa, Pisa, Italy, in 2006 and 2010, respectively.

In 2009, he was a Visiting Researcher at the Department of Radio Science and Engineering, Aalto University, Espoo, Finland. From 2015 to 2017, he was a short-term Visiting Researcher with the Grenoble Institute of Technology, Valance, France, and University Rovira I Virgili, Tarragona, Spain. He is currently with the University of Pisa. His current research interests include metamaterials, metasurfaces, antennas, and radio frequency identification.

Dr. Costa was a recipient of the Young Scientist Award of the URSI International Symposium on Electromagnetic Theory, URSI General Assembly, and URSI AT-RASC, in 2013, 2014, and 2015, respectively. He serves as an Associate Editor for IEEE TRANSACTIONS ON ANTENNAS AND PROPAGATION, IEEE ANTENNAS AND WIRELESS PROPAGATION LETTERS, IEEE SENSORS LETTERS, *Scientific Reports*, and *Sensors and Electronics*.